Applied Surface Science 581 (2022) 152094

Contents lists available at ScienceDirect

Applied Surface Science

journal homepage: www.elsevier.com/locate/apsusc

Full Length Article

Electric field-induced electronic-thermoelectric-optical properties of typical isoelectronic HNC_6 monolayers: A theoretical study

Niladri Sekhar Mondal [a], Subhadip Nath [b], Suman Chowdhury [c], Debnarayan Jana [d,*]

[a] Department of Physics, Haldia Government College, Haldia 721657, India
[b] Department of Physics, Krishnagar Government College, Krishnagar 741101, India
[c] Skolkovo Institute of Science and Technology, Skolkovo Innovation center, 3 Nobel Street, Moscow 121205, Russia
[d] Department of Physics, University of Calcutta, 92 A. P. C. Road, Kolkata 700009, India

ARTICLE INFO

Keywords:
Dirac materials
Electric field
Thermoelectric properties
Optical properties

ABSTRACT

Using the combined first-principles, tight-binding, and machine-learning interatomic potential approaches, we explore the electric field effects on the electronic, thermoelectric, and optical properties of buckled hexagonal isoelectronic HNC_6 monolayers, a member of HAC_6 (A = N, P, As) family. These material(s) possess a Dirac cone in their band structure which can be attributed to the same electron count of every site (C/N) and the presence of a weak π bond between carbon and nitrogen atoms. We predict that a transverse electric field can induce a tunable bandgap, the gap is nearly proportional to the electric field strength, suitable for use in the electronics industry. The thermoelectric performance of HNC_6 is better than graphene, which can be further improved by the application of an external electric field. The region of the chemical potential for the optimal thermoelectric performance can also be tuned by the electric field. The Wiedemann–Franz ratio deviates from that of ordinary metals and is nearly twice that of graphene and four times that of universal value. For parallel polarization, HNC_6 shows pronounced optical response in the infrared and visible region. Plasma frequencies appear in the visible regions which are blue-shifted with electric field strength. The P and As counterpart of HNC_6 shows similar electronic, thermoelectric, and optical properties on the application of electric field, with thermoelectric performance even superior to HNC_6. These intriguing electronic, thermoelectric, and optical properties in presence of an electric field suggest great potential of HAC_6 for novel electronic, energy harvesting, and optoelectronic devices.

1. Introduction

Graphene and its exquisite electronic, thermal, optical, and mechanical properties [1–6] fascinate researchers both in theory and experiment. The novel properties of graphene lie in its unique band structure (BS) exhibiting Dirac cones at the Fermi level [5]. Graphene being a gapless semi-metal, its potential for applications in present-day nano-devices is somewhat restricted. Thus various methods, namely chemical functionalization [7], introduction of defects [8] and dopants [9], strain [10], application of electric fields [11] have been employed to introduce a finite gap in the energy dispersion at the Dirac point. Nonetheless, these methods were not been adequately progressed for fundamental and technological purposes. In the quest for new promising two-dimensional (2D) materials, group IV-V systems got great attention [12–15], among them carbon-based compounds are found to be more stable than others [16]. Typically the lattices with hexagonal symmetry or its topological equivalent are mostly found to have Dirac cones.

Recently H.Y. Lu et al. proposed a family of HAB_6 (A = N, P, As, Sb, Bi; B = C, Si, Ge, Sn) monolayers possessing Dirac cones on symmetry lines [17]. Intuitively they followed the electron-counting rule [18] by hydrogenating the P atom of PC_6 monolayers [19] and converting it to a semi-metal, which is otherwise a direct-gap semiconductor. In PC_6 the C—C bonds are sp^2 hybridized as graphene and P—C bonds are sp^3 hybridized, one sp^3 orbital on the P atom contains an electron pair. Upon hydrogenation, these P atoms form an H-P covalent bond, with every site (C/P) of the 2D plane having the same electron count as graphene. Though, due to sp^3 hybridization of P atoms, π bonds between P—C will be much weaker than C—C π bonds.

Two points about HAB_6 monolayers are interesting, firstly the presence of Dirac cone at K points, secondly the buckled structure with

* Corresponding author.
E-mail address: djphy@caluniv.ac.in (D. Jana).

https://doi.org/10.1016/j.apsusc.2021.152094
Received 8 September 2021; Received in revised form 19 November 2021; Accepted 28 November 2021
Available online 20 December 2021

hexagonal symmetry. In nanostructures with a finite thickness/buckling, the commonly used technique to precisely manipulate the Dirac cone is the application of a transverse external electric field [16,20]. Since HAB_6 has buckled structure, we expect that its electronic structure will behave similarly. Graphene-like high carrier mobility along with bandgap flexibility can present HAB_6 suitable for applications in nano and opto-electronics devices.

In this paper, we explore the electronic, thermoelectric, and optical properties of hexagonal carbon-based group IV-V HAC_6 (A = N, P, As) monolayers in presence of an external transverse electric field. Our focus is mainly on HNC_6, a Dirac material from HAB_6 family unless otherwise stated. We organized the paper as follows: In the next section, we present the computational details used for the investigation of the different properties of the structure(s). We also propose a tight-binding (TB) model Hamiltonian that efficiently demonstrates the emergence of Dirac cone at K points. In the 'Result and Discussion' section, we first study the electronic properties of HNC_6 both in the presence and absence of an external electric field. In this regard, an effective Hamiltonian is considered for TB calculations and compared to the first principle calculations. Next, we consider the thermoelectric and optical properties of the structures with and without the application of external perturbation. Finally, we briefly discuss the salient features of the P and As counterpart of HNC_6.

2. Computational methods

2.1. First principle calculation

We have performed our density functional theory (DFT) calculations implemented with the Quantum ESPRESSO package (QE) [21,22]. A projector augmented wave (PAW) technique [23,24] is utilized to treat the ion–electron interaction. The exchange–correlation energy of the electrons is treated via the generalized gradient approximation within the scheme of Perdew-Burke-Ernzerhof (GGA-PBE) [25]. The kinetic energy cutoff for the wave function and charge density is taken as 50 Ry and 600 Ry, respectively. To avoid any spurious interactions between two neighboring HAC_6 layers, a sufficiently large vacuum space (15 Å) is kept between the layers. The Brillouin zone (BZ) is sampled with a uniform $16 \times 16 \times 1$ Monkhorst–Pack (MP) [26] special k grid points for the structural optimization. The geometry of the sheets is optimized until the residual forces on each atom are converged below 0.01 eV/Å. For the electronic, thermoelectric, and optical properties a sufficiently dense $36 \times 36 \times 1$ k-point mesh is used.

Better representation of the potential energy surface has always been an important issue for the scientific community while performing atomistic simulations or experiments. Nowadays machine-learning models are being used extensively in the field of materials science as it computes complex functions easily [28]. In the present work, the DFT calculations have been replaced by the moment tensor potential (MTP) [29]. Here MTP belongs to the machine-learning interatomic potentials (MLIP) [30–34] families. It offers a flexible functional form having an incredibly high level of accuracy. The situation is quite similar to classical potentials where the parameters are optimized on a set of training configurations. Here the training sets are created by employing *ab-initio* molecular dynamics (AIMD) simulations. At the initial stage, MTP shows its effectiveness while dealing with single-component systems [29], but in the later stage it has been successfully applied in multi-component systems [35,36]. Here local potential is being used i.e. the total energy E of the system is partitioned into contributions V of neighborhoods u_i of each i-th atom: $E \equiv E^{MTP} = \sum_{i=1}^{N} V(u_i)$, where N is the total number of atoms. Here the j-th atom is referred to be the neighbor of the i-th (central) atom if the distance between them is less than a predefined cut-off distance R_{cut}. The neighborhood then can be expressed as the following collection,

$$u_i = (\{r_{i1}, z_i, z_1\}, \ldots, \{r_{ij}, z_i, z_j\} \ldots, \{r_{iN_{nei}}, z_i, z_{N_{nei}}\}) \quad (1)$$

where r_{ij} are the relative atomic positions (interatomic vector), z_i and z_j are the types of the central and neighboring atoms respectively and N_{nei} is the number of atoms in the neighborhood. Each one of the contribution to the total energy has the following form: $V(u_i) = \sum_\alpha \xi_\alpha B_\alpha(u_i)$, where ξ_α are the free parameters of the potential to be optimized and B_α are the basis functions. We construct the basis functions as all possible contractions of the following moment tensor descriptors:

$$M_{\mu,\nu}(r_i) = \sum_{j=1}^{N_{nei}} f_\mu(|r_{ij}|, z_i, z_j) r_{ij}^{\otimes \nu} \quad (2)$$

which yields a scalar [29]. The first factor $f_\mu(|r_{ij}|, z_i, z_j)$ within the summation is the radial part which depends only on the distance between atoms i and j and their types. If we expand the radial part through a set of radial basis functions $\phi_\beta(|r_{ij}|)$ multiplied by a factor $(R_{cut} - |r_{ij}|)^2$ for smoothing near the cut-off radius, then we will have the following form:

$$f_\mu(|r_{ij}|, z_i, z_j) = c^{(\beta)}_{\mu, z_i, z_j} \quad (3)$$

here $c^{(\beta)}_{\mu, z_i, z_j}$ are the radial coefficients. The outer product is denoted by the symbol " $\otimes$ " referring to the second factor of Eq. 2 as the angular part. Now to optimize the ξ_α and $c^{(\beta)}_{\mu, z_i, z_j}$ parameters of an MTP, one needs to minimize the following problem (training of MTP):

$$\sum_{k=1}^{K} w_e \left(E_k^{AIMD} - E_k^{MTP}\right)^2 + w_f \sum_{i}^{N} |f_{k,i}^{AIMD} - f_{k,i}^{MTP}|^2 + w_s \sum_{i,j=1}^{3} |\sigma_{k,ij}^{AIMD} - \sigma_{k,ij}^{MTP}|^2 \rightarrow min \quad (4)$$

here $E_k^{AIMD}, f_{k,i}^{AIMD}$ and $\sigma_{k,ij}^{AIMD}$ are the energy, atomic forces and stresses in the training set respectively and $E_k^{MTP}, f_{k,i}^{MTP}$ and $\sigma_{k,ij}^{MTP}$ are the corresponding values calculated with the MTP. K is the number of the configurations in the training set and w_e, w_f and w_s are the non-negative weights that denote the importance of energies, forces, and stresses in the optimization problem respectively. In this work we have taken the values of w_e, w_f and w_s are 1, 0.1 and 0.001 respectively. Here readers are encouraged to look into Ref. [37] for further details about the guide to create the training set, the procedure to calculate MTP forces, and for all the example files of that work. In this work, the phonon spectra have been calculated in two ways to check the validation and the accuracy of the MTP employed for these systems: i) by using density functional perturbation theory (DFPT) which were carried out over $2 \times 2 \times 1$ supercell using a $2 \times 2 \times 1$ k-point mesh. After this stage, PHONOPY [27] package was employed to obtain the phonon dispersion curves and the second-order harmonic force constants. ii) The force calculations have been done by using MTP and then we have used the PHONOPY [27] package to obtain the phonon dispersion curves. In Fig. S1 of the ESI, we have depicted the phonon spectra using both methods. It can be observed that the MLIP results are almost identical to the DFPT results. This proves the validity as well as the quality of our machine-learning potentials. The use of MTP has been proven to be quite successful in predicting new novel materials [35,38], in order to study lattice dynamics [37,39,40] and for calculating thermal conductivities [41–43] of various systems. In some of the very recent studies [37,44], it has been demonstrated that MTPs trained over short MD trajectories can accurately reproduce the phononic properties of various 2D materials compared to the DFT simulations. Following Ref. [37], the training sets are being prepared by conducting AIMD simulation within the GGA functional for 2000 time steps at 50 K and 100–700 K over $2 \times 2 \times 1$ supercell using a $2 \times 2 \times 1$ k-point grid with a time step of 1 fs. The lattice part of the thermal conductivity calculations is performed by the full iterative solution of the Boltzmann transport equation as implemented within the ShengBTE [45] package. During calculations of the lattice thermal conductivity, the most challenging part is to evaluate the anharmonic (third-order) force constants, which normally need several

hundred single point DFT calculations. But here MTPs are fitted passively that has replaced the computationally expensive DFT simulations for the anharmonic force constants calculations. In this work, we have used the same number of supercells as those employed while doing the DFPT calculations. Besides, we have considered up to the seventh nearest neighbors interaction to determine the lattice thermal conductivity. Electronic transport properties e.g. Seebeck coefficient, electrical conductivity, electronic thermal conductivity are calculated by solving the semiclassical Boltzmann transport equation within the constant relaxation time approximation as implemented in the BoltzTraP code [46], which involves the solution of the semi-classical Boltzmann transport equation (BTE) within the constant relaxation time approach and rigid band approximation. The electrical conductivity ($\sigma_{\alpha\beta}$), Seebeck coefficient ($S_{\alpha\beta}$) and electronic thermal conductivity ($\kappa^{e}_{\alpha\beta}$) tensors are expressed in terms of temperature (T) and chemical potential μ as [46]:

$$\sigma_{\alpha\beta}(T,\mu) = \frac{1}{\Omega}\int \sigma_{\alpha\beta}(\varepsilon)\left[-\frac{\partial f_{\mu}(T,\epsilon)}{\partial\varepsilon}\right]d\varepsilon \tag{5}$$

$$S_{\alpha\beta}(T,\mu) = \frac{1}{eT\sigma_{\alpha\beta}(T,\mu)}\int \sigma_{\alpha\beta}(\varepsilon)(\varepsilon-\mu)\left[-\frac{\partial f_{\mu}(T,\epsilon)}{\partial\varepsilon}\right]d\varepsilon \tag{6}$$

$$\kappa^{e}_{\alpha\beta}(T,\mu) = \frac{1}{\Omega e^{2}T}\int \sigma_{\alpha\beta}(\varepsilon)(\varepsilon-\mu)^{2}\left[-\frac{\partial f_{\mu}(T,\epsilon)}{\partial\varepsilon}\right]d\varepsilon \tag{7}$$

where α and β represent the tensor indices. The symbols $\varepsilon(k), \tau(k), f, e$ and Ω represents the band energy, relaxation time, Fermi function, electronic charge and volume of the cell, respectively.

The reliability of the relaxation time approximation is well established in previous studies [46–49]. This approximation has been extensively used in several studies to solve the Boltzmann equation, which transforms the integrodifferential equation to a numerically simpler differential equation. The evaluation of the relaxation time (τ) is required for calculation. However, since experimental data related to τ is not available, we present the scaled values of all the transport properties with temperature keeping τ as a fixed parameter.

The optical properties of the systems were calculated with the random phase approximation (RPA) approach using Troullier-Martins type [50,51] norm-conserving (NC) pseudo-potentials with PBE exchange–correlation and kinetic energy cutoff for the wave function of 60 Ry. The optical properties of a medium can be fully described by the complex dielectric $\epsilon_{\alpha,\beta}(\omega)$ function given by

$$\epsilon_{\alpha,\beta}(\omega) = \epsilon_{1_{\alpha,\beta}}(\omega) + i\epsilon_{2_{\alpha,\beta}}(\omega) \tag{8}$$

$$\begin{aligned} &= 1 + \frac{4\pi e^{2}}{\Omega N_{\mathbf{k}} m^{2}}\sum_{n,n'}\sum_{\mathbf{k}}\frac{\langle u_{\mathbf{k},n'}\left|\widehat{\mathbf{p}}_{\alpha}\right|u_{\mathbf{k},n}\rangle\langle u_{\mathbf{k},n}\left|\widehat{\mathbf{p}}^{\dagger}_{\beta}\right|u_{\mathbf{k},n'}\rangle}{\left(E_{\mathbf{k},n'}-E_{\mathbf{k},n}\right)^{2}} \\ &\times\left\{\frac{f(E_{\mathbf{k},n'})}{E_{\mathbf{k},n'}-E_{\mathbf{k},n}+\hbar\omega+i\hbar\Gamma}+\frac{f(E_{\mathbf{k},n'})}{E_{\mathbf{k},n'}-E_{\mathbf{k},n}-\hbar\omega-i\hbar\Gamma}\right\} \end{aligned} \tag{9}$$

where Γ is the *intersmear* broadening parameter and ω is the frequency of the incident light in eV. The real and the imaginary part of the dielectric function is related to each other by the Kramers–Kronig transformation [52].

The electron energy loss spectrum (EELS) is proportional to the imaginary part of the inverse dielectric function, given by

$$L(\omega) = Im\left\{-\frac{1}{\epsilon_{\alpha,\beta}(\omega)}\right\} = \frac{\epsilon_{2_{\alpha,\beta}}(\omega)}{\epsilon^{2}_{1_{\alpha,\beta}}(\omega)+\epsilon^{2}_{2_{\alpha,\beta}}(\omega)} \tag{10}$$

We have considered a large number of empty bands ($N_{bands} > 100$) for the optical properties calculation for more accurate responses. We are keen on the investigation of the optical properties of the systems utilizing DFT as a computationally inexpensive method.

2.2. Tight-binding model

We present an effective nearest-neighbor (NN) TB Hamiltonian that parametrizes the energetic description of the lattice in the vicinity of the Fermi energy.

$$H_{0} = \epsilon_{C}\sum_{i\in C}c^{\dagger}_{i}c_{i} + \epsilon_{N}\sum_{i'\in N}c^{\dagger}_{i'}c_{i'} + \sum_{i,j\in C}t_{ij}\left(c^{\dagger}_{i}c_{j}+h.c.\right) + \sum_{i'\in N,j\in C}t_{i'j}\left(c^{\dagger}_{i'}c_{j}+h.c.\right) \tag{11}$$

where $\epsilon_{C}(\epsilon_{N})$ is the on-site energy of site C(N) atoms, $t_{ij}(t_{i'j})$ is the hopping integral connecting nearest-neighbor C,C (N,C) sites.

To investigate the effect of the transverse electric field, we incorporate the following term in Eq. (11),

$$H_{E} = \frac{eE}{2}\sum_{i\in C,i'\in N}\left(z_{i}c^{\dagger}_{i}c_{i} + z_{i'}c^{\dagger}_{i'}c_{i'}\right) \tag{12}$$

where e is the electron charge, E is the transverse electric field, $z_{i}(z_{i'})$ are the z-coordinates of the C(N) atoms. Therefore, in the presence of an external electric field, the total Hamiltonian of the system now reads as:

$$H = H_{0} + H_{E} \tag{13}$$

3. Results and discussions

3.1. Structural details and verification

The optimized crystal structure of HNC_6 monolayer is shown in Fig. 1 (a). The unit cell, which has hexagonal symmetry, comprises 2 H, 2 N, and 12 C atoms. This structure can also be viewed as a hydrogenated-nitrogen-doped graphene structure, with the position of hydrogenated-nitrogen forming a large hexagon as shown in the figure. It is composed of C_6 ring surrounded by six NC_5 rings. The lattice constant for the structure is 6.5012 Å, which is very close to the previously predicted value [17]. Since the buckling of the adjacent hydrogenated-N atoms is in opposite direction concerning the carbon plane, this lattice structure can be considered as having three layers (Fig. 1(b)) with buckling of Δz = 0.87 Å, between two adjacent N atoms. The buckling distance between N atoms is higher than silicene ($\Delta z \sim 0.50$ Å) and germanene ($\Delta z \sim 0.70$ Å) [53]. Four different bond lengths in the 2D plane can be realized owing to two non-equivalent positions of C atoms, labeled as C1 (carbon atoms in the C_6 rings) and C2 (carbon atoms adjacent to N atoms). The different bond lengths of this structure are detailed in Table 1.

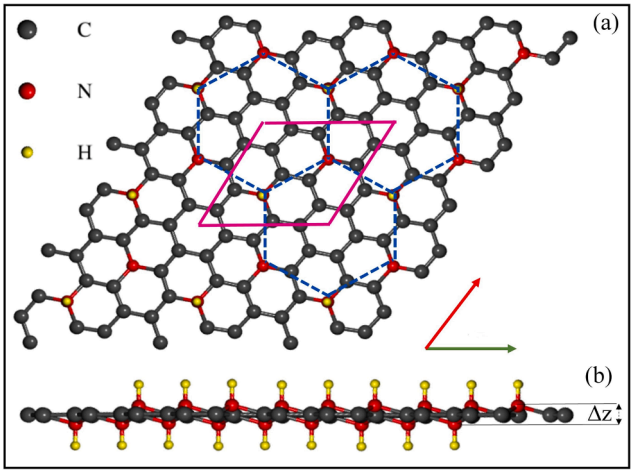

Fig. 1. Optimized structure of 3 × 3 supercell of HNC_6 with (a) top and (b) side view. The unit cell is marked with the parallelogram. The blue dotted line connects the hydrogenated-N atoms forming a large hexagon.

Table 1
Different bond length (Å), their orientation w.r.t. $X-Y$ plain and the hopping amplitude ($t's$) (eV) between different atoms in the HNC_6 monolayer.

Parameters	N-C2	C1-C1	C1-C2	C2-C2	N-H
bond length	1.508	1.424	1.399	1.396	1.049
Orientation	$\sin^{-1}(0.282)$	$\sin^{-1}(0.012)$	$\sin^{-1}(0.012)$	$\sin^{-1}(0.013)$	-
Hopping Amplitude	$-0.60(=t_4)$	$-2.31(=t_1)$	$-2.44(=t_2)$	$-2.40(=t_3)$	-

As reported in Ref. [17], this structure is stable at the ground state with no imaginary phonon frequency. The molecular dynamics study reveals that the atomic structure is thermodynamically stable at a temperature of 400 K. Also, the structure is mechanically stable.

The formation energy is also calculated using $\Delta E = (2E_{HNC_6} - E_{H_2} - 2E_{NC_6})/2$, where ΔE is the formation energy. This formula is defined according to the chemical equation $2NC_6 + H_2 \rightarrow 2HNC_6$. The calculated value of the formation energy is -1.8618 eV per unit cell. The negative sign of the formation energy also confirms the stability of the HNC_6 structure.

3.2. Salient features of electronic properties

We first investigate the electronic band structure (BS) and projected density of states (PDOS) of HNC_6 monolayers and is depicted in Fig. 2. The band structure is evaluated along the high symmetry path $\Gamma \rightarrow M \rightarrow K \rightarrow \Gamma$ of the irreducible BZ. The valence band maximum and conduction band minimum touch each other at K high-symmetric point. The total DOS at the Fermi level is zero which further confirms the existence of the Dirac cone. The charge carriers of the system behaves as massless Dirac fermions with Fermi velocity $v_F = \frac{1}{\hbar}\frac{dE}{dk}|_{\vec{k}\rightarrow\vec{K}} = 5.64 \times 10^5$ and 6.31×10^5 m/s along $K \rightarrow M$ and $K \rightarrow \Gamma$ directions.

We now explore the inherent morphology of this structure and emergence of the Dirac cones using the TB model as given in Eq. (11). The Eq. (11) can be solved by diagonalization of a 14×14 matrix in the reciprocal space [54] for obtaining the energy dispersion curves. In solving the TB Hamiltonian we have considered only the C and N atoms. Here we argue that H atoms in the structure are in a valence saturation state, whereas there is one extra electron in each N/C site, which contributes to the energy band calculation. We represent NN hopping as t_1, t_2, t_3 and t_4 for NN C1—C1, C1—C2, C2—C2 and N—C2 bonds, respectively. We consider only the energy states near the Fermi level. The DFT generated low energy band is best fitted with the TB results (Fig. 2) taking $t_1 = -2.31, t_2 = -2.44, t_3 = -2.40$ and $t_4 = -0.60$ eV. The on-site energy of N and C atoms are taken as 1.35 and -1.05 eV respectively to set the Fermi level at zero. Small value of t_4 (nearly 25 percent of t_1, t_2, t_3) reflects weak π bonding between N and C atoms. The PDOS calculations also reveal that p_z orbitals of C atoms mainly contribute near the Fermi level. Nonetheless, hydrogenated N atoms conserve the same electron count at every site, and the weak π bonds between N and C might be responsible for the Dirac cone which is otherwise absent in NC_6. The Dirac cone is robust under the variation of hopping energy. It remains intact and there is no shifting or splitting of the Dirac cone along the k-path. However, the Dirac point gets shifted along the vertical line through K high-symmetric point as the hopping strength is varied. Notably, it moves upward for $|t_4| < 0.60$ eV and downward for $|t_4| > 0.60$ eV.

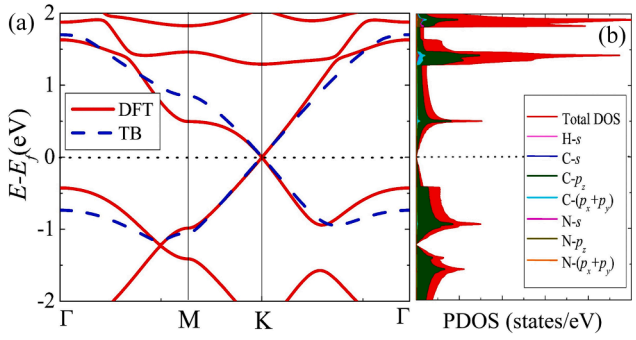

Fig. 2. (a) The electronic BS of HNC_6 calculated by both DFT (solid red lines) and TB (broken blue lines) method. The Fermi level is set to zero. Only the upper valence band and lower conduction band are shown for TB calculations. (b) The projected density of states spectrum.

3.2.1. Effect of transverse electric field

The buckling nature of HNC_6 allows studying the effect of the transverse electric field on the electronic properties by both DFT and TB. The application of a transverse electric field breaks the reflection symmetry, resulting in a bandgap opening. We have varied the electric field in the range of 0–1 V/Å. With the application of electric field, the Dirac cones at the K high symmetric point begin to split, and a small direct bandgap emerges. The linear bands at the Fermi level now gradually transform into parabolic ones. The calculated BS and DOS for $E = 0.5$ and 1.0 V/Å are shown in Fig. 3(a-b), respectively. The bandgap is found to increase with the magnitude of the applied field and is depicted in Fig. 4a. Interestingly, the bandgap tuning by an external electric field is possible only due to the buckling, which enters through N atoms, otherwise planar structures do not allow this band modulation. The bandgap calculated by DFT calculation is parabolic, while that for TB is almost linear. This behavior may arise due to the screening effect of the hydrogenated-N atom, which is not considered in the TB method. The screening effect arises due to the polarization of charges with the rise of the electric field. This in turn screens the external electric field [11]. The rate of bandgap opening ($\frac{dE_g}{dE}$) is not constant and is ~ 0.07 eÅ and 0.22 eÅ at small and large electric field, respectively.

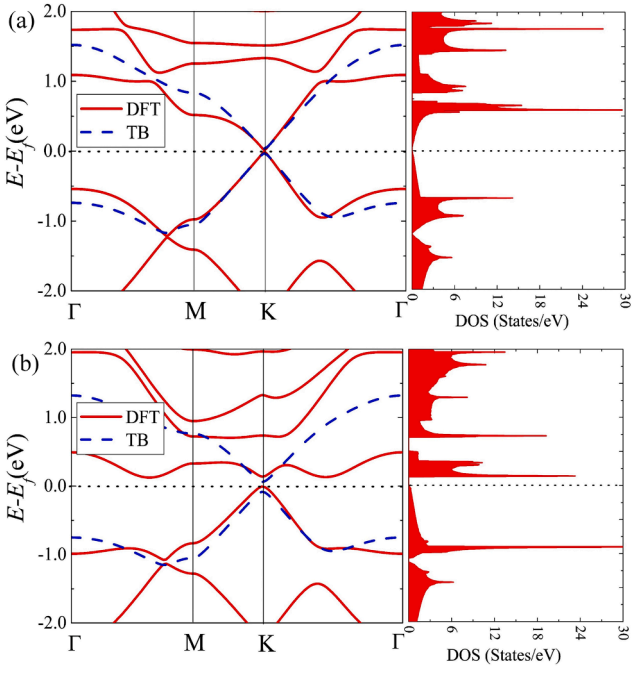

Fig. 3. (a) The electronic BS of HNC_6 for (a) $E = 0.5$ V/Å and (b) $E = 1.0$ V/Å calculated by DFT (solid red lines) and TB (broken blue lines) along with the DOS spectrum. The Fermi level is set to zero.

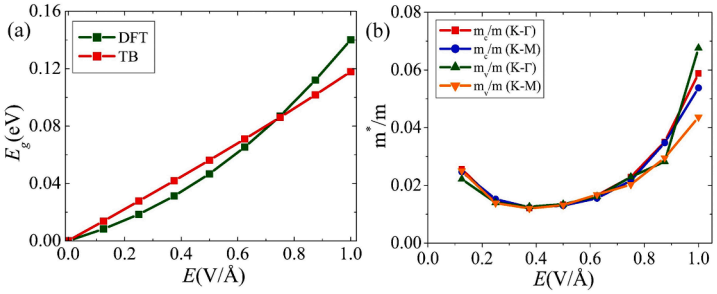

Fig. 4. (a) Bandgap E_g vs. electric field E calculated by DFT and TB method. (b) Effective mass of electrons and holes (m_c and m_v, respectively) with E along the direction $K-\Gamma$ and $K-M$.

We have calculated the direction-dependent effective mass of the electrons and holes (m_c and m_v) of the structure in different electric fields by the quadratic polynomial fitting of the conduction and valence bands and is shown in Fig. 4b. Results show that the effective mass of both carriers and in direction $K\rightarrow\Gamma$ and $K\rightarrow M$ are nearly the same and indicate a parabolic nature with the minimum of the effective mass occurring at $E = 0.375$ V/Å. This behavior may arise due to non-linear change of the conduction band minimum and valence band maximum point (at K-high symmetric point) during the deformation of BS by the external field. This result is contrary to that obtained by Ni et al. using the TB method, which predicts a universal linear behavior [11]. The calculated minimum values of effective masses are $m_c^{K\Gamma}$=0.0122m, m_c^{KM}=0.0124m, $m_v^{K\Gamma}$=0.0127m and m_v^{KM}=0.0120m, where m is the rest mass of free electron. We have also roughly estimated the mobility of the charge carriers of the unperturbed system and at the electric field $E =$ 0.375 V/Å, using the relation $\mu_m = e\tau/m^*$. Using this relation and considering the relaxation time to be in the order of graphene [55], the mobility of carriers in HNC_6 is 10^5 $cm^2V^{-1}s^{-1}$. This is of the same order of mobility of suspended graphene ($\mu_m \sim 20{,}000$ $cm^2V^{-1}s^{-1}$) [56].

Since the thermoelectric and optical properties of a material depend on its band structure, which in turn can be modified by an electric field, both the properties also can be tuned in the presence of an external electric field. In the next two subsections, we explore the thermoelectric and optical properties of HNC_6 in the presence of an electric field.

3.3. Thermoelectric properties

Recently, exploring new thermoelectric materials, are of great interest due to their ability to directly convert heat into electricity and vice versa with significant potential in industrial application [57–60]. The thermoelectric performance of the material is typically measured by different interconnected properties like electrical conductivity (σ), Seebeck coefficient (S), Power factor (σS^2), the dimensionless thermoelectric figure of merit (ZT). The position of chemical potential (μ) along with temperature plays a pivotal role in transport properties. The decisive factor for determining which electrons in the valence or conduction bands take part in the electronic transport is dictated by the position of μ in the band structure, which can be manipulated by doping or substitution. Chemical potential is determined by the temperature and by the total number of carriers. The difference between chemical potential and Fermi energy $\mu - E_f$ is positive (negative) for electron (hole) doping.

3.3.1. Electrical conductivity

In Fig. 5(a-c), we have plotted the electrical conductivity divided by relaxation time (σ/τ) as a function of chemical potential at fixed temperatures for applied electric field $E = 0.0$, 0.5 and 1.0 V/Å, respectively. At zero electric field the electrical conductivity shows nearly symmetric behaviour at the vicinity of the Fermi level E_f similar to the DOS spectrum. Due to the injection of carriers, σ/τ increases with the chemical potential and reaches maximum at a certain value for both n- and p-doped regions. The electrical conductivity for the p-doped region is more pronounced than the n-doped region. The maximum value of σ/τ obtained at room temperature are $\sim 6.643 \times 10^{19}$ and $\sim 4.830 \times 10^{19}$ $\Omega^{-1}m^{-1}s^{-1}$ at $\mu - E_f = -0.827$ and 0.813 eV, respectively. Moreover, at the vicinity of the Fermi level σ/τ also increases with temperature due to thermal excitations. At $\mu \rightarrow E_f$, σ/τ shows a small value and the values obtained are $\sim 5.010 \times 10^{16}$ and $\sim 1.701 \times 10^{18}$ $\Omega^{-1}m^{-1}s^{-1}$ at 100 and 700 K, respectively.

In the presence of a finite external electric field, the behavior of the electric conductivity becomes asymmetric. The DOS spectrum shows a gapped behavior (zero DOS) around $\mu - E_f$ =0.0 and 0.6 eV, which is reflected in the electrical conductivity spectrum. The electrical conductivity at these narrow regions is vanishingly small and is of the order of $\sim 10^{14}$ $\Omega^{-1}m^{-1}s^{-1}$ at 100 K. At sufficiently high temperatures the excited electrons and/or holes contribute to the conductivity. The peak positions in the electrical conductivity are consistent with the Van Hove singularities, as also reported in previous studies [61]. While σ/τ reaches a maximum value in the p-doped region for $E = 0.5$ V/Å, it reaches the maximum value (though outside the range of interest) at the n-doped region for $E = 1.0$ V/Å. The maximum value of the σ/τ in presence of a transverse electric field for both n- and p- doped regions are tabulated in Table 2.

3.3.2. Seebeck coefficient

Seebeck coefficient (S) is an important parameter determining the efficiency of a thermocouple. It also indicates the type of dominant carriers in a material: for p-type S is positive, while S is negative for n-type materials. We have shown the variation of S with chemical potential at different temperature for $E = 0.0$, 0.5 and 1.0 eV/Å in Fig. 6(a-c), respectively. In the absence of an electric field, the Seebeck coefficient shows two pronounced peaks at the vicinity of the Fermi level for n-/p- type HNC_6, which indicates that an efficient thermoelectric efficiency can be achieved at optimal carrier concentration. With the rise in temperature, however, the coefficient degrades due to the bipolar conduction effect i.e. the excitation of positive and negative charge carriers [62]. The maximum of S obtained for hole-doped regime is 188.0 μVK^{-1} (at $\mu - E_f$=-0.017) and 139.4 μVK^{-1} (at $\mu - E_f$=-0.113) at $T = 100$ and 700 K, respectively. For electron-doped regime the values are 140.4 μVK^{-1} ($\mu - E_f$=0.017), 109.8 μVK^{-1} ($\mu - E_f$=0.119) at $T = 100$ and 700 K respectively. This suggests better performance at the hole-doped regime in absence of perturbation.

The application of an external electric field increases the Seebeck coefficient significantly. Moreover, both the peaks in the vicinity of the Fermi level tend to shift towards the n-type region. At sufficiently large electric field ($E = 1.0$ V/Å) and low temperature T <300 K, both the peaks appear at the electron-doped regime. The behavior of the Seebeck coefficient can be explained with the DOS spectrum: The Seebeck coefficient is zero when the chemical potential is at the middle of the valence and conduction band, as the electron and hole currents compensate each other. As $\mu - E_f$ moves towards the valence band or conduction band, the number of states accessible for transport is

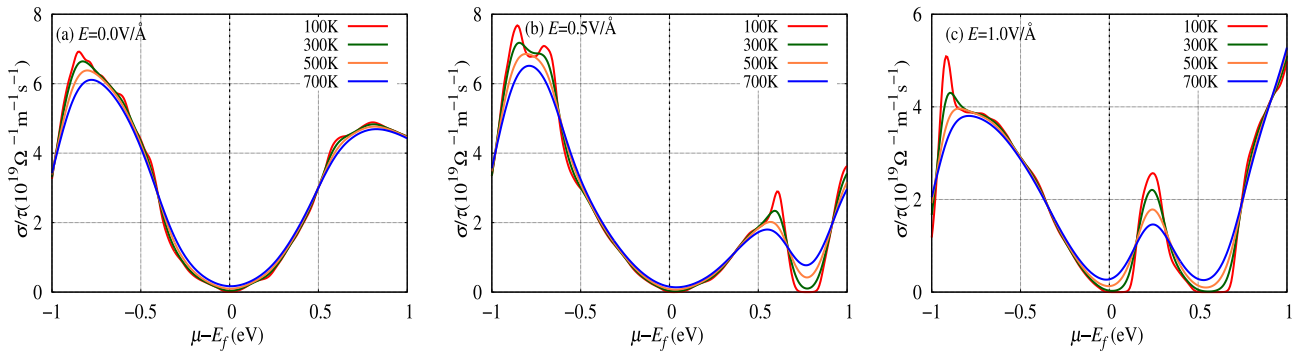

Fig. 5. Variation of the electrical conductivity σ/τ with chemical potential $\mu - E_f$ at $T = 100$, 300, 500, 700 K for electric field strength (a) E = 0.0 V/Å (b) E = 0.5 V/Å (c) E = 1.0 V/Å.

Table 2
Estimated bandgap and maximum values of different thermoelectric properties for p- and n- doped region in presence of applied electric field at room temperature.

E(V/Å)	E_g(eV)	$\sigma/\tau(\times 10^{19})(\Omega^{-1}m^{-1}s^{-1})$		$S(\mu VK^{-1})$		$PF(\times 10^{10})(W/mK^2s)$		ZT_{el}	
		p-doped	n-doped	p-doped	n-doped	p-doped	n-doped	p-doped	n-doped
0.00	0.000	6.643	4.830	133.7	−128.8	5.86	6.48	0.377	0.349
0.25	0.019	7.013	3.959	154.0	−144.3	10.31	5.00	0.447	0.394
0.50	0.047	7.177	2.340	185.0	−166.5	10.69	5.44	0.547	0.467
0.75	0.087	6.995	2.018	243.3	−225.9	13.34	12.56	0.678	0.573
1.00	0.140	4.302	2.206	184.9	−316.1	2.82	15.16	0.487	0.740

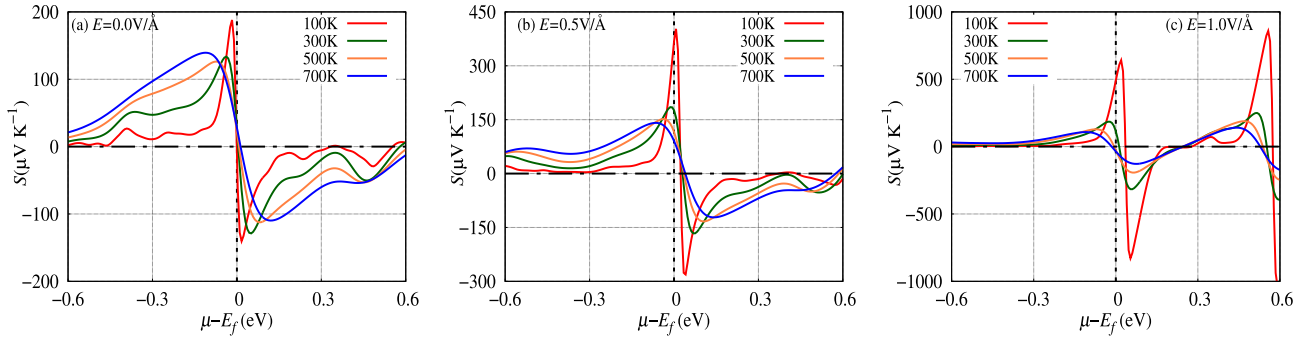

Fig. 6. Variation of the Seebeck coefficient (S) with chemical potential $\mu - E_f$ at $T = 100$, 300, 500, 700 K for (a)$E = 0.0$ V/Å (b) $E = 0.5$ V/Å (c) $E = 1.0$ V/Å.

different on either side of Fermi energy, resulting in a large Seebeck coefficient. The magnitude of the Seebeck coefficient is strongly dependent on the bandgap and increases with the gap. Due to the same reason, the Seebeck coefficient also shows large values at the region around $\mu - E_f \sim 0.6$ eV for $E = 1.0$ V/Å.

3.3.3. Power factor

One of the keynote quantities for investigating the thermoelectric efficiency is the power factor divided by relaxation time τ, defined as $PF = S^2\sigma/\tau$. The calculated values of the PF is shown in Fig. 7(a-c) for $E = 0.0$, 0.5 and 1.0 eV/Å, respectively. In the absence of an electric field and at low temperature ($T \leqslant 300$ K), the PF for the n-type region is higher than the p-type region. However, with the increase in temperature, the PF for the

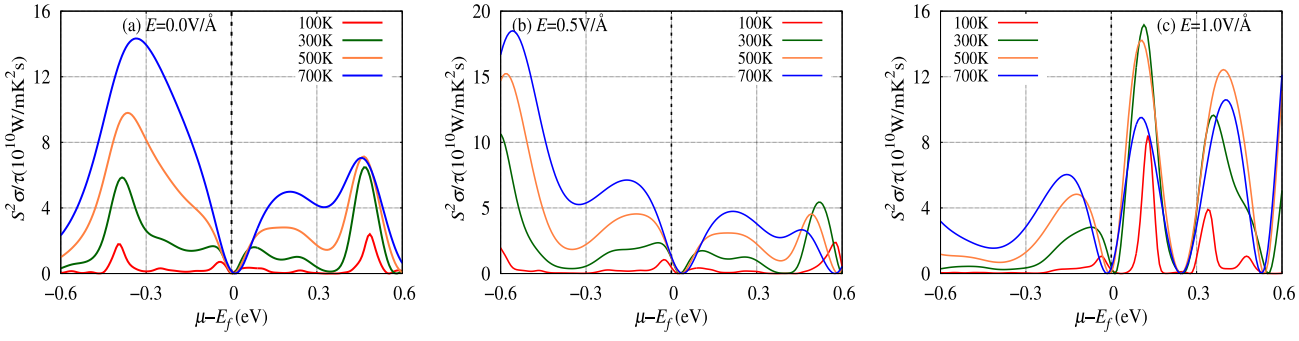

Fig. 7. Variation of the Power factor (PF) with chemical potential $\mu - E_f$ at $T = 100$, 300, 500, 700 K for (a)$E = 0.0$ V/Å (b) $E = 0.5$ V/Å (c) $E = 1.0$ V/Å.

p-type region is significantly larger than the n-type region. The calculated maximum power factor for HNC_6 at 100 K is 17.91×10^9 and 24.01×10^9 W/mK^2s for p- and n- doped region, respectively. At 700 K, the calculated values are 143.32×10^9 and 70.05×10^9 W/mK^2s, respectively. The maximum of the PF arises due to the better trade-off between the Seebeck coefficient and electrical conductivity. The minimum of the PF is obtained for chemical potential where the Seebeck coefficient reverses its sign.

The PF can be largely improved by the presence of external perturbation. Additionally, the magnitude of the electric field also decides, whether HNC_6 will perform better as n-doped or p-doped. For example, up to $E\leqslant0.75$ V/Å the system performs better when p-doped, while n-doped regions show superior PF at $E = 1.0$ V/Å.

3.3.4. Wiedemann Franz law and Figure of Merit

We have calculated the Wiedemann–Franz (WF) ratio for HNC_6 structure for both in the presence and absence of an electric field. The WF law for ordinary metals states that, $\kappa_e/\sigma T = \mathscr{L}$ =constant, where $\mathscr{L}$ is the Lorentz number. For ordinary metals $\mathscr{L} = \mathscr{L}_0 = \pi^2k_B^2/3e^2 = 2.44\times10^{-8}\ W\Omega K^2$. In Fig. 8, we have plotted $\kappa_e/\sigma T$ with temperature for $E = 0.0$, 0.5, 1.0 V/Å. This value is also independent of relaxation time τ. The Lorentz number $\mathscr{L}$ is nearly constant for $E = 0.0$V/Å and is $\sim 9.441\times10^{-8}\ W\Omega K^{-2}$. This value is nearly twice that of graphene ($\mathscr{L}_G = 5.79\times10^{-8}\ W\Omega K^{-2}$) [63], and four times that of the universal value $\mathscr{L}_0$. These higher values of $\mathscr{L}$ can be attributed to the unusual nature of the band structure with Dirac fermions. In presence of an electric field, $\mathscr{L}$ is not constant and is dependent on temperature. Similar behavior is already predicted for materials with a gap[64]. Moreover, the values are higher than the unperturbed system.

The efficiency of a thermoelectric material in a energy conversion process is determined by the dimensionless figure of merit (ZT) defined as,

$$ZT = \frac{\sigma S^2 T}{\kappa_{el} + \kappa_L} \tag{14}$$

$$ZT = \frac{\sigma S^2 T}{\kappa_{el}}\left(\frac{1}{1+\kappa_L/\kappa_{el}}\right) = \frac{ZT_{el}}{1+\kappa_L/\kappa_{el}} \tag{15}$$

where $ZT_{el} = \sigma S^2 T/\kappa_{el}$ is the electronic figure of merit, which provides the maximum value of the total figure of merit, and does not include the phononic contribution to the thermal conductivity. κ_{el} and κ_L is the thermal conductivity due to the electrons and lattice (phonons). The BoltzTraP code only calculates the electronic thermal conductivity and hence only information about ZT_{el} can be obtained from this code.

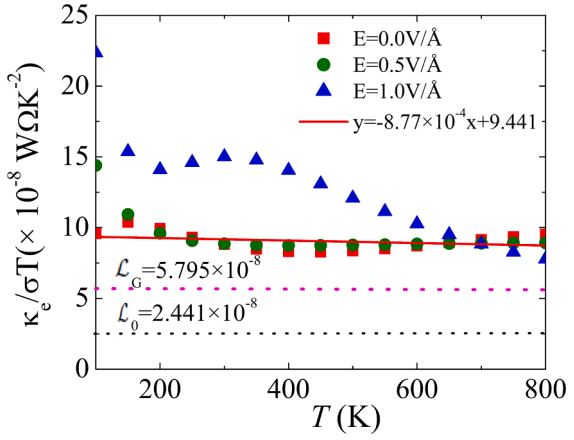

Fig. 8. Temperature dependence of $\kappa_e/\sigma T = \mathscr{L}$ for $E = 0.0$, 0.5, 1.0 V/Å. The red line represents the least square fit for the pristine unperturbed system. The black and magenta dotted line represents the universal value of Lorentz number ($\mathscr{L}_0$) and the value of $\mathscr{L}$ for graphene ($\mathscr{L}_G$).

However, we have used a machine-learning interatomic approach to evaluate the lattice thermal conductivity which will shed light on the value of ZT of this material. Generally, high electrical conductivity and Seebeck coefficient, and low thermal conductivity will lead to large ZT_{el}. In Fig. 9, we have shown the electronic figure of merit *vs.* chemical potential for different values of an external electric field. For the unperturbed system, $ZT_{el} = 0.377$ and 0.349 at room temperature. Moreover, for $E = 0.0$ V/Å, $ZT_{el} \propto S^2$, by virtue of Wiedemann–Franz ratio, $\mathscr{L}$, which is nearly constant. A decrease in temperature increases ZT_{el}, however, it is known that thermal conductivity is mainly dominated by κ_L at low temperature, hence it can be anticipated that $ZT \ll ZT_{el}$.

In Fig. 10, we have depicted the lattice thermal conductivity of the HNC_6 system as a function of temperature. We have also fitted the κ_L curves (see Fig. 10) to check the accurate temperature dependency. From the figures, it can be concluded that κ_L nearly maintains an inverse relationship with the temperature. The lattice thermal conductivity of HNC_6 77.47 W/mK, while for pristine graphene it is 14.1 W/mK (taking $\tau = 3.0\times10^{-13}$sec for graphene) [66]. In the ESI, we have also shown (see Fig. S3) the variation of κ_{el} for better comparison. Results suggest that the electronic part of thermal conductivity increases with temperature. However, increased electrical conductivity and the Seebeck coefficient lead to higher ZT than graphene. At much higher temperature $\kappa_{el} > \kappa_L$ and hence $ZT \lesssim ZT_{el}$. The electronic figure of merit is found to increase with the applied electric field and at $E = 1.0$ V/Å, ZT_{el} is greater than unity at low temperature (T=100 K). The calculated values of ZT_{el} at the room temperature for different applied electric fields for both n- and p-doping are tabulated in Table 2. The system will perform better when hole-doped at a small electric field ($E\leqslant0.75$ V/Å), an electron-doped at a sufficiently large electric field. We have also compared the maximum values of different thermoelectric properties of pristine HNC_6 at room temperature with other 2D materials and are summarized in Table 3. However, taking into account the lattice thermal conductivity the value of the figure of merit is reduced to 0.02 at room temperature. The figure of merit tabulated in the table mainly provides the electronic contribution and is less in nearly all cases. Clearly, this structure shows better thermoelectric performance than graphene and can be more improved by applying a transverse electric field.

3.4. Optical properties

The electronic property of any system plays a pivotal role in determining its optical properties. The tuning of the electronic properties by the application of a transverse electric field motivates us to investigate the optoelectronic properties of the system. We calculated the frequency-dependent optical properties like $\epsilon_2(\omega), \epsilon_1(\omega), L(\omega)$ of the systems in presence of both the transverse external electric field and polarised electromagnetic field. The optical properties have been calculated in the three directions of polarization *viz.* *x*-, *y*-, and z-direction. Due to structural anisotropy $\epsilon^x = \epsilon^y \neq \epsilon^z$, we present result only for the parallel ($E_p \| x$ or y) [1] and perpendicular ($E_p \perp x$ or $E_p \| z$) type.

In Fig. 11(a) and (b), we present the imaginary part of the dielectric function ($\epsilon_2(\omega)$) as a function of photon energy (ω) in presence of external applied electric field for $E_p \| x$ and $E_p \perp x$, respectively. The dielectric function is prominent in the frequency range ω= 0–4 eV and 0–18 eV for $E_p \| x$ and $E_p \perp x$, respectively. A strong anisotropy is observed in the optical response between the two types of polarization due to the two-dimensional nature. The imaginary part of the dielectric function shows a major peak around $\omega \sim 0.12$ eV, which is slightly blue-shifted with the rise of E. Further, the intensity of this peak decrease with the applied field strength. A minor peak also emerges with the increase of electric field ($E\geqslant0.5$ eV/Å) in the IR region. The peak positions reported are 1.42, 1.22 and 1.08 eV for $E = 0.5$, 0.75 and 1.0 eV/Å, respectively.

[1] We have used E_p to represent the electric field of the incident polarised light, and E for the applied external electric field.

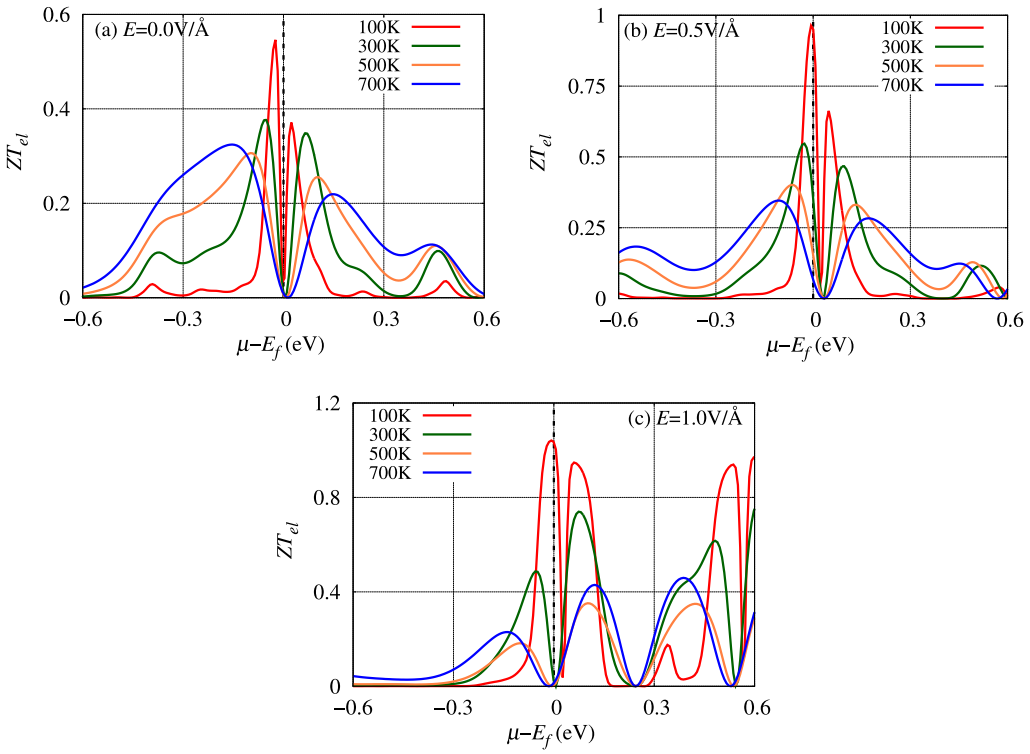

Fig. 9. Variation of the electronic Figure of merit (ZT_{el}) with chemical potential $\mu - E_f$ at $T = 100$, 300, 500, 700 K for (a)$E = 0.0$ V/Å (b) $E = 0.5$ V/Å (c) $E = 1.0$ V/Å.

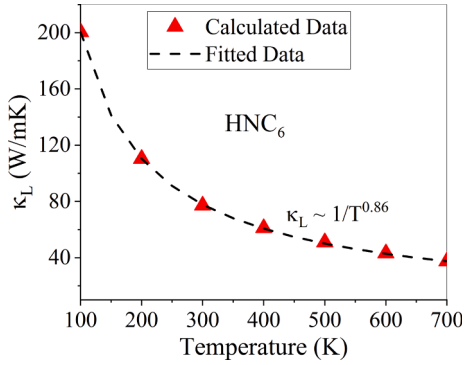

Fig. 10. Lattice thermal conductivity (κ_L) of HNC_6 as a function of temperature.

Table 3
Comparative study of the various thermoelectric properties of few 2D materials at room temperature.

Structure[Ref.]	σ/τ ($\Omega^{-1}m^{-1}s^{-1}$)	$S(\mu VK^{-1})$	$S^2\sigma/\tau$ (W/mK^2s)	ZT
Graphene [66]	0.33×10^{19}	31	0.3×10^{10}	0.08
Silicene [67]	-	-	-	0.36*
Germanene [67]	-	-	-	0.41*
T-Silicene [68]	4.52×10^{19}	73	9.3×10^{10}	0.16*
MoS_2 [69]	1.25×10^{19}	550	42.0×10^{10}	0.70
Be_3C_2 [61]	2.96×10^{19}	151	2.68×10^{10}	0.33*
HNC_6†	6.64×10^{19}	134	6.48×10^{10}	0.38*
HPC_6†	10.71×10^{19}	234	14.1×10^{10}	0.64*
$HAsC_6$†	9.54×10^{19}	392	14.2×10^{10}	0.86*

† This work.
* Indicates electronic figure of merit ZT_{el}.

These peaks normally arise due to π-π^* band transition. The HNC_6 structure shows no response in the UV region of the EM spectrum. For $E_p \perp z$, several peaks are observed for $\epsilon_2(\omega)$. In absence of an external electric field, two prominent peaks appear at 2.42 and 13.84 eV. The first peak may arise due to $\pi - \pi^*$ interband transition, while the broad second peak is due to $\sigma - \sigma^*$ transition. The application of electric field splits the first peak into two peaks: A sharp low energy peak appears at ω=1.02 −1.68 eV, while the other appears at ω=2.38–3.28 eV. The lower energy peaks are red-shifted, while the other peak is blue-shifted with the increase of the external electric field. Further, the intensity of the sharp peak increases with E. At $E = 1.0$ V/Å, the low energy second peak again tends to split into two similar peaks at 2.92 eV and 3.28 eV. The broad peak in the far UV region appears in the frequency range ω=13.52 −13.84 eV. The strong response of $\epsilon_2(\omega)$ in the IR region suggests that this material may find its application in the solar cell.

The real part of the dielectric function provides information about the amount of energy stored in the system and plays a key role in determining the collective role of free electrons. The variation of $\epsilon_1(\omega)$ with frequency for different applied electric field is shown in Fig. 12(a) and (b) for both parallel and perpendicular polarization, respectively. Our study reveals that the static real part of the dielectric constant for $E_p \| x$ is large ($\epsilon_1(0) \sim 28.89$) for the pristine system in absence of an electric field. This value is nearly 8 times larger than pristine graphene [65]. With the application of the electric field E, $\epsilon_1(0)$ decreases and reaches ~ 22.14 for $E = 1.0$ V/Å. Contrary, $\epsilon_1(0)$ for $E_p \perp x$ increases with the applied electric field and is much smaller than $E_p \| x$. The calculated values for E = 0.0, 0.25, 0.5, 0.75 and 1.0 V/Å are $\epsilon_1(0)$=1.61, 1.77, 2.06, 2.44 and 2.84, respectively. The presence of a large number of free carriers results in non-zero $\epsilon_1(0)$. The decrease in $\epsilon_1(0)$ by application of electric field can be attributed to the transition from semi-metallic to semiconducting characteristics. Thus this carbon-based material has a significantly higher value of $\epsilon_1(0)$ and can be tuned by the application of an electric field. For both polarization, the dielectric function increases beyond the zero-frequency limit to its maximum value and then sharply decreases. $\epsilon_1(\omega)$ then has few noticeable fluctuations and ultimately

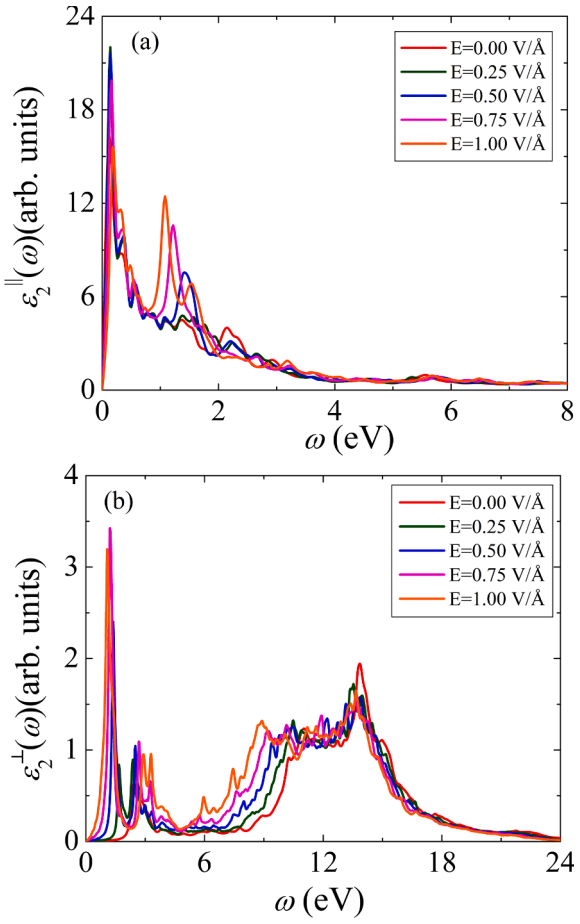

Fig. 11. Imaginary part of the dielectric function $\epsilon_2(\omega)$ as a function of photon energy ω for (a) $E_p \| x$ (b) $E_p \perp x$.

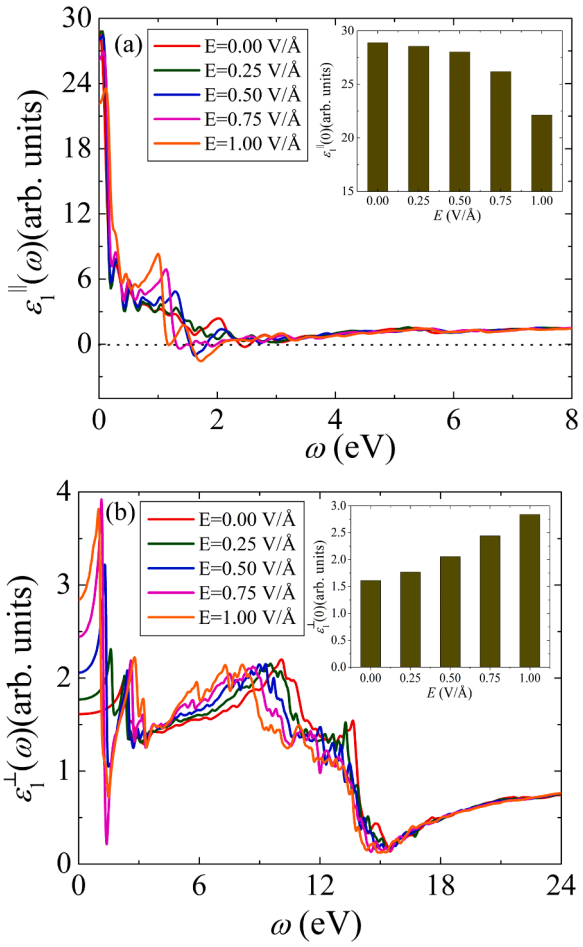

Fig. 12. Real part of the dielectric function $\epsilon_1(\omega)$ as a function of photon energy ω for (a) $E_p \| x$ (b) $E_p \perp x$.

becomes smooth. A negative value of the real part is observed in the far IR to the visible region of the EM spectrum for only parallel polarization which denotes the optically metallic character of HNC_6. The intensity of the peak in the negative region increases with E.

The plasma frequencies (ω_p), which corresponds to the collective excitation of the electrons, can be predicted from the peak in the EELS curve, which corresponds to plasmon resonance. The EEL spectrum is depicted in Fig. 13. The EELS shows a major peak in the visible region of the EM spectrum, with few small surrounding minor peaks for $E_p \| x$. The calculated plasma frequency for parallel polarization are ω_p=3.26, 3.36, 3.44, 3.76, 3.40 eV for E = 0.0, 0.25, 0.50, 0.75, 1.0 V/Å. A strong intensity peak is also evinced for perpendicular polarization in the far UV region, along with a few minor sharp peaks in the IR region to the visible region. The plasma frequencies for both parallel and perpendicular polarization are tabulated in Table 4.

4. Salient features of other carbon-based isoelectronic structures

Similar to HNC_6 monolayers, HPC_6 and $HAsC_6$ shows similar structural and electronic properties with N replaced by P and As. These two structures are also stable as predicted by Lu et al. [17] and possesses Dirac points at the K-high symmetric point (Fig. 14a) with maximum Fermi velocity 5.97 $\times 10^5$ m/s and 6.23 $\times 10^5$ m/s, respectively. Since these structures are also buckled, the application of an external electric field leads to a bandgap opening at the K point. However, the gap opening is smaller than HNC_6 and decreases with the atomic weight of the group-V element. For all the structures the gap increases with the external field, though a drop in bandgap while going beyond 0.8 V/Å in

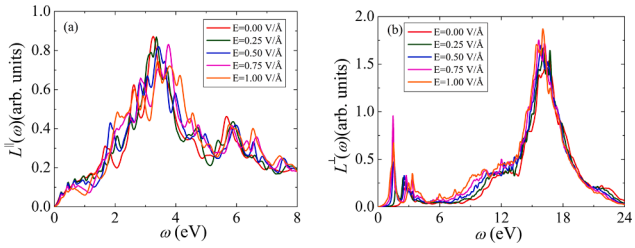

Fig. 13. Electron energy loss spectra (EELS) $L(\omega)$ as a function of photon energy ω for (a) $E_p \| x$ (b) $E_p \perp x$.

Table 4
Plasma frequency (ω_p in eV) for HNC_6 structure for different electric field (E in V/Å) for parallel ($E_p \| x$) and perpendicular ($E_p \perp x$) polarizations.

E	$E_p \| x$	$E_p \perp x$
0.0	3.26	2.48, 16.65
0.25	3.36	1.72, 2.66, 16.08, 16.72
0.50	3.44	1.50, 2.54, 15.87
0.75	3.76	1.46, 2.74, 15.65
1.0	3.40	1.50, 3.34, 16.05

the case of $HAsC_6$ is notable. This may be due to the high atomic weight of As, at a high electric field outer electrons could be disrupted which effectively reduces the polarization due to the electric field and hence the decrease in the bandgap. We have shown the variation of bandgap

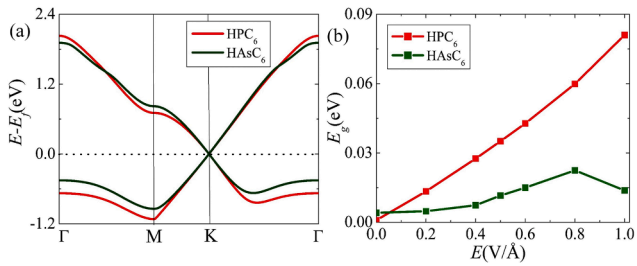

Fig. 14. (a) Band structure of HPC_6 and $HAsC_6$ in absence of electric field. Only the upper valence band and lower conduction band are shown. (b) Bandgap E_g vs. applied electric field E calculated by DFT.

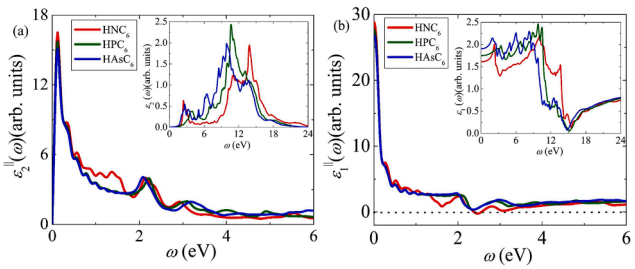

Fig. 15. Imaginary part of the dielectric function ($\epsilon_2(\omega)$) vs. energy(ω) for (a)$E_p \| x$ and (b) $E_p \perp x$.

with applied external electric field in Fig. 14b. We have further studied the thermoelectric properties of the HPC_6 and $HAsC_6$ structures in absence of an electric field. The maximum values of the thermoelectric parameters are tabulated in Table 3. These two structures also perform better when hole-doped. Moreover, the thermoelectric performance of the materials is largely improved by altering the group-V element i.e. increases with the increase of atomic weight. For example, the calculated electronic figure of merit for 0.64 and 0.86 for HPC_6 and $HAsC_6$, respectively at room temperature. In the Electronic Supplementary Information (ESI), we have also shown (see Fig. S2) the κ_L values for the other two systems. From the Figures, it can be noticed that the lattice thermal conductivity is highest for the $HAsC_6$ system and lowest for the HNC_6 system. This is due to the mass difference. Here the most massive system is the $HAsC_6$ system because of the presence of As atoms and the least massive is the HNC_6 system because of N. Generally more massive the system is, less its lattice thermal conductivity. This trend is visible here. Considering the lattice thermal conductivity, the figure of merit is 0.04 and 0.18 for HPC_6 and $HAsC_6$, respectively. Similar to HNC_6, also both the structures show better thermoelectric performance with the application of an electric field.

We have also determined the optical response of HPC_6 and $HAsC_6$, in terms of $\epsilon_2(\omega)$ for both $E_p \| x$ and $E_p \perp x$ in Fig. 15. Both the structures show similar optical responses with HNC_6. The peak in the IR region for $E_p \| x$ appears at the same frequency, with the intensity slightly decreasing with the atomic weight of B-atom. For $E \perp x$, the peak height of HPC_6 is maximum and the peak position of HNC_6 and $HAsC_6$ lies on either side of HPC_6. Since all other optical properties are calculated from ϵ_2, we can expect that the behavior of other properties will also show a similar response like HNC_6.

The intriguing electronic, thermoelectric, and optical properties of these monolayers may be interesting for experimentalists and find their application in nanoelectronic, energy conversion, and optical devices.

5. Conclusion

In summary, we systematically examine the effect of transverse electric field on the electronic, thermoelectric and optical properties of buckled hexagonal HNC_6 monolayers. We employ both first-principle calculation as well as a tight-binding model to tune the band by the perturbation. In the absence of perturbation, HNC_6 is a semi-metal with a Dirac cone at K point, and Dirac point is rather robust with the variation of hopping energy. With the application of electric field, both DFT and TB calculations show bandgap opening, which increases with the field strength. The N atoms play a crucial role in the existence of the Dirac cone as well as in the band-gap opening. The electrical conductivity, the figure of merit, and the power factor of the unperturbed HNC_6 are found to be much higher than graphene at room temperature, which suggests HNC_6 as a better material for its performance in thermoelectric devices over graphene. The application of electric field largely improves the thermoelectric properties of HNC_6. The electric field strength also determines whether the system will behave better when p- or n- doped. The structure shows a strong optical response in the IR and visible region for parallel polarization, while for perpendicular polarization the response is in the IR and deep UV region. A sharp peak in ϵ_2 appears in the IR region for both types of polarization. A small peak in $\epsilon_2(\omega)$ appears in the visible region for $E_p \| x$ with the application of electric field and are red-shifted with the field strength. The major plasma frequency appears in visible region for $E_p \| x$, while in the IR and deep UV region for $E_p \perp x$. The P and As analogue of HNC_6 also show similar behavior with more improved thermoelectric properties. In the presence of an electric field, the thermoelectric performance of these two materials rises substantially. The optical properties of these classes of hexagonal HAC_6 materials show similar behavior. All these intriguing properties of HAC_6 materials may be interesting for experimentalists for their synthesis and application in different nano-devices.

Author Contribution Statement

NSM: Simulations, Formal Analysis, Writing original draft. **SN**: Conceptualization, Simulations, Formal Analysis, Writing original draft. **SC**: Simulation, Formal Analysis, Writing Revised draft, **DJ**: Conceptualization, Formal Analysis, Discussions, Finalizing manuscript.

Declaration of Competing Interest

The authors declare that they have no known competing financial interests or personal relationships that could have appeared to influence the work reported in this paper.

Acknowledgment

NSM and SN thank Supriya Ghosal, University of Calcutta for stimulating discussions. SC would like to thank Skolkovo Institute of Science and Technology for providing computational resources.

Appendix A. Supplementary material

Supplementary data associated with this article can be found, in the online version, at https://doi.org/10.1016/j.apsusc.2021.152094.

References

[1] K.S. Novoselov, A.K. Geim, S.V. Morozov, D. Jiang, Y. Zhang, S.V. Dubonos, I. V. Grigorieva, A.A. Firsov, Science 306 (2004) 666.
[2] K.S. Novoselov, A.K. Geim, S.V. Morozov, D. Jiang, M.I. Katsnelson, I. V. Grigorieva, S.V. Dubonos, A.A. Firsov, Nature (London) 438 (2005) 197.
[3] A.K. Geim, K.S. Novoselov, Nat. Mater 6 (2007) 183.
[4] C. Lee, X.D. Wei, J.W. Kysar, J. Hone, Science 321 (2008) 385.
[5] A.K. Geim, Science 324 (2009) 1530.
[6] A.H. Castro Neto, F. Guinea, N.M.R. Peres, Rev. Mod. Phys. 81 (2009) 109–162.
[7] S. Chowdhury, D. Jana, Rep. Prog. Phys. 79 (2016) 126501.
[8] M. Ali, X. Pi, Y. Liu, D. Yang, AIP Adv. 7 (2017) 045308.
[9] P. Nath, S. Chowdhury, D. Sanyal, D. Jana, Carbon 73 (2014) 275.
[10] S. Deng, A.V. Sumanty, V. Berry, Nano Today 22 (2018) 14.
[11] Z. Ni, Q. Liu, K. Tang, J. Zheng, J. Zhou, R. Qin, Z. Gao, D. Yu, J. Lu, Nano Lett. 12 (2012) 113.
[12] C. Barreteau, B. Michon, C. Besnard, E. Giannini, J. Cryst. Growth 443 (2016) 75.

[13] C.S. Jung, D. Kim, S. Cha, Y. Myung, F. Shojaei, H.G. Abbas, J.A. Lee, E.H. Cha, J. Park, H.S. Kang, J. Mater. Chem. A 6 (2018) 9089.
[14] Y. Jing, Y. Ma, Y. Li, T. Heine, Nano Lett. 17 (2017) 1833.
[15] A. Len, W. Orellana, E.S. Morell, M. Pacheco, Phys. Rev. B 101 (2020) 085408.
[16] V. Kumar, K. Rajput, D.R. Roy, Carbon 172 (2021) 791.
[17] H.Y. Lu, N. Jiao, B.W. Li, W.C. Yi, P. Zhang, Appl. Sur. Sci. 554 (2021) 149635.
[18] M.S. Miao, J. Botana, E. Zurek, T. Hu, J. Liu, W. Yang, Chem. Mater. 28 (2016) 1994.
[19] T. Yu, Z. Zhao, Y. Sun, A. Bergara, J. Lin, S. Zhang, H. Xu, L. Zhang, G. Yang, Y. Liu, J. Am. Chem. Soc. 141 (2019) 1599.
[20] S. Ghosal, A. Bandyopadhyay, D. Jana, Phys. Chem. Chem. Phys. 22 (2020) 19957.
[21] P. Giannozzi, et al., J. Phys.: Condens. Matter 21 (2009) 395502.
[22] P. Giannozzi, et al., J. Phys.: Condens. Matter 29 (2017) 465901.
[23] P.E. Blöchl, Phys. Rev. B 50 (1994) 17953.
[24] A. Dal Corso, Comput. Mater. Sci. 95 (2014) 337.
[25] J.P. Perdew, K. Burke, M. Ernzerhof, Phys. Rev. Lett. 77 (1996) 3865.
[26] H.J. Monkhorst, J.D. Pack, Phys. Rev. B 13 (1976) 5188.
[27] A. Togo, I. Tanaka, Scr. Mater. 108 (2015) 1.
[28] E. Bedolla, L.C. Padierna, R. Castañeda-Priego, J. Phys: Condens. Matter 33 (2020) 053001.
[29] A.V. Shapeev, Multiscale Model. Simul. 14 (2016) 1153.
[30] K. Schutt, P.J. Kindermans, H.E.S. Felix, S. Chmiela, A. Tkatchenko, K.R. Muller, Adv. Neural Inf. Process. Syst. (2017) 991.
[31] V. Botu, R. Batra, J. Chapman, R. Ramprasad, J. Phys. Chem. C 121 (2017) 511.
[32] Y. Zuo, C. Chen, X. Li, Z. Deng, Y. Chen, J. Behler, G. Csanyi, A.V. Shapeev, A. P. Thompson, M.A. Wood, S.P. Ong, J. Phys. Chem. A 124 (2020) 731.
[33] B. Mortazavi, E.V. Podryabinkin, I.S. Novikov, T. Rabczuk, X. Zhuang, A. V. Shapeev, Comp. Phys. Commun. 258 (2021) 107583.
[34] B. Mortazavi, E.V. Podryabinkin, S. Roche, T. Rabczuk, X. Zhuang, A.V. Shapeev, Mater. Horiz. 7 (2020) 2359.
[35] K. Gubaev, E.V. Podryabinkin, G.L.W. Hart, A.V. Shapeev, Comput. Mater. Sci. 156 (2019) 148.
[36] K. Gubaev, E. Podryabinkin, A.V. Shapeev, J. Chem. Phys. 148 (2018) 241727.
[37] B. Mortazavi, I.S. Novikov, E.V. Podryabinkin, S. Roche, T. Rabczuk, A.V. Shapeev, X. Zhuang, Appl. Mater. Today. 20 (2020) 100685.
[38] E.V. Podryabinkin, E.V. Tikhonov, A.V. Shapeev, A.R. Oganov, Phys. Rev. B. 99 (2019) 064114.
[39] V.V. Ladygin, P.Y. Korotaev, A.V. Yanilkin, A.V. Shapeev, Comput. Mater. Sci. 172 (2020) 109333.
[40] I.S. Novikov, A.S. Shapeev, Mater. Today Commun. 18 (2019) 74.
[41] P. Korotaev, I. Novoselov, A. Yanilkin, A. Shapeev, Phys. Rev. B. 100 (2019) 144308.
[42] B. Mortazavi, E.V. Podryabinkin, I.S. Nvikov, S. Roche, T. Rabczuk, X. Zhuang, A. V. Shapeev, J. Phys. Condens. Mater. 3 (2020) 02LT02.
[43] M. Raeisi, B. Mortazavi, E.V. Podryabinkin, F. Shojaei, X. Zhuang, A.V. Shapeev, Carbon 167 (2020) 51.
[44] S. Ghosal, S. Chowdhury, D. Jana, Phys. Chem. Chem. Phys. 23 (2021) 14608.
[45] W. Li, J. Carrete, N.A. Katcho, N. Mingo, Comput. Phys. Commun. 185 (2014) 1747.
[46] G.K. Madsen, D.J. Singh, Comput. Phys. Commun. 175 (2006) 67.
[47] R. Chmielowski, D. Pere, C. Bera, I. Opahle, W. Xie, S. Jacob, F. Capet, P. Roussel, A. Weidenkaff, G.K.H. Madsen, G. Dennler, J. Appl. Phys. 117 (2015) 125103.
[48] H. Shi, D. Parker, M.-H. Du, D.J. Singh, Phys. Rev. Appl. 3 (2015) 014004.
[49] G. Dennler, R. Chmielowski, S. Jacob, F. Capet, P. Roussel, S. Zastrow, K. Nielsch, I. Opahle, G.K.H. Madsen, Adv. Energy Mater. 4 (2014) 1301581.
[50] N. Troullier, J.L. Martins, Phys. Rev. B. 43 (1991) 8861.
[51] M. Fuchs, M. Scheffler, Comput. Phys. Commun. 119 (1999) 67.
[52] S. Nath, A. Bandyopadhyay, S. Datta, Md. Mohi Uddin, D. Jana, Physica E 120 (2020) 114087.
[53] S. Cahangirov, M. Topsakal, E. Aktürk, H. Sahin, S. Ciraci, Phys. Rev. Lett 102 (2009) 236804.
[54] N.S. Mondal, S. Nath, D. Jana, N.K. Ghosh, J. Phys. Chem. Solids 150 (2021) 109801.
[55] W. Choi, H. Nishiyama, Y. Ogawa, Y. Ueno, K. Furukawa, T. Takeuchi, Y. Tsutsui, T. Sakurai, S. Seki, Adv. Optical Mater. 6 (2018) 1701402.
[56] K.I. Bolotin, K.J. Sikes, Z. Jiang, M. Klima, G. Fudenberg, J. Hone, P. Kim, H. L. Stormer, Sol. Stat. Commun. 146 (2008) 351.
[57] S. Nolas, J. Sharp, H.J. Goldsmid, Thermoelectrics: Basic Principles and New Materials Developments, Springer Series in Material Science vol. 45, Springer-Verlag, Berlin, 2001.
[58] H.J. Goldsmid, Springer Series in Material Science, 1st ed., Springer-Verlag, Berlin, 2010, p. 250.
[59] F.J. DiSalvo, Science 285 (1999) 703.
[60] C. Vining, Nat. Mater. 8 (2009) 83.
[61] S. Nath, J. Appl. Phys. 130 (2021) 055106.
[62] H. Shi, D. Parker, M.-H. Du, D.J. Singh, Phys. Rev. Appl. 3 (2015) 014004.
[63] M. Inglot, A. Dyrdal, V.K. Dugaev, 1 Barnaś Phys, Rev. B 91 (2015) 115410.
[64] A. Rycerz, Materials 14 (2021) 2704.
[65] R. John, B. Merlin, J. Phys. Chem. Solids 110 (2017) 307.
[66] A.H. Reshak, S.A. Khan, S. Auluck, J. Mat. Chem. C 2 (2014) 2346.
[67] K. Yang, S. Cahangirov, A. Cantarero, A. Rubio, R. S'Agosta, Phys. Rev. B. 89 (2014) 125403.
[68] N.S. Mondal, S. Nath, D. Jana, N.K. Ghosh, Phys. Chem. Chem. Phys. 23 (2021) 11863.
[69] J. Hong, C. Lee, J.-S. Park, J.H. Shim, Phys. Rev. B 93 (2016) 035445.